ADVANCED MATERIALS

DOI: 10.1002/adma.200600310

Simultaneously Increasing the Ductility and Strength of Nanostructured Alloys**

By *Yong-Hao Zhao*, *Xiao-Zhou Liao*, *Sheng Cheng*, *En Ma*, and *Yuntian T. Zhu**

Strength and ductility are two of the most important mechanical properties of structural materials. However, they are often mutually *exclusive*, i.e., a material may be strong or ductile, but rarely both at the same time.[1] This is also true for bulk nanostructured materials,[2] which usually have high strength, but disappointingly low ductility.[2,3] Bulk nanostructured materials are usually synthesized by either a two-step approach such as nanopowder consolidation,[4,5] or a one-step approach such as severe plastic deformation.[6,7] The latter approach can synthesize flaw-free nanostructured materials with higher ductility than those synthesized by nanopowder consolidation. However, even these nanostructured materials often exhibit a very low uniform elongation (strain before necking). Uniform elongation should be used as a measure of the ductility of nanostructured materials because it is much less affected by the gauge length than the elongation to failure. The latter gives a false impression of high ductility in samples with very short gauge length (e.g., less than 5 mm, as used in many studies) due to large post-necking strain.

A high work-hardening rate is essential for good uniform elongation because it can help delay localized deformation (necking) under tensile stress.[8] Bulk nanostructured materials often have a very low or no work-hardening rate because of their low dislocation accumulation capability.[9–11] Indeed, there has been considerable effort to address the pressing need of increasing the ductility of nanostructured materials at room temperature, but all the previous attempts to this end have sacrificed some of their yield strengths gained from nanostructuring.[9,12,13]

In this paper we report a strategy to *simultaneously* increase the ductility and strength of bulk nanostructured materials. By engineering very small second-phase particles into a nanostructured Al alloy matrix, we were able to more than double its uniform elongation, while further gaining rather than sacrificing its yield strength. The simultaneous enhancement of ductility and strength is due to the increased dislocation accumulation and resistance to dislocation-slip by second-phase particles, respectively. Our strategy is applicable to many nanostructured alloys and composites, and paves a way for their large-scale industrial applications.

The material used in this model study is 7075 Al alloy. The alloy was solution-treated to obtain a coarse-grained (CG) solid solution. The CG sample was immediately cryogenically rolled to produce nanostructures with an average grain size of ca. 100 nm (designated as NS sample). The NS sample was then aged at low temperature to introduce very small second-phase particles (designated as NS+P sample).

The engineering stress–strain curves of these samples are compared in Figure 1a. The 0.2 % yield strengths (marked by circles) of the CG, NS, and NS+P samples are 145 MPa, 550 MPa, and 615 MPa, respectively. Therefore, the low-temperature aging enhanced the yield strength of the NS sample by 12 %. The uniform elongation (marked by the symbol □ on the curves in Fig. 1a) was determined by the Considère criterion (Eq. 1) governing the onset of localized deformation[8]

$$\left(\frac{\partial\sigma}{\partial\varepsilon}\right)_{\dot{\varepsilon}} = \sigma \tag{1}$$

where σ is the true stress and ε is the true strain. As shown, the uniform elongation of the NS sample is only 3.3 %. In contrast, the uniform elongation of the NS+P sample is 7.4 %, which is more than twice that of the NS sample and above the critical ductility (5 %) required for many structural applications. The enhanced ductility of the NS+P sample was caused by an improved work-hardening rate, Θ, defined by Equation 2

$$\Theta = \frac{1}{\sigma}\left(\frac{\partial\sigma}{\partial\varepsilon}\right)_{\dot{\varepsilon}} \tag{2}$$

As shown in Figure 1b, the NS+P sample has a higher Θ than the NS sample. The work hardening factors, n, defined by Equation 3

$$\sigma = K\varepsilon^{n} \tag{3}$$

where K is a constant, are 0.35, 0.11, and 0.15 for the CG, NS, and NS+P samples, respectively.

[*] Dr. Y. T. Zhu, Dr. Y. H. Zhao
Materials Science and Technology Division
Los Alamos National Laboratory
MS G755, Los Alamos, NM 87545 (USA)
E-mail: yzhu@lanl.gov
Dr. X.-Z. Liao
The James Franck Institute
University of Chicago
5640 South Ellis Avenue
Chicago, IL 60637 (USA)
Dr. S. Cheng, Prof. E. Ma
The Department of Materials Science and Engineering
Johns Hopkins University
Baltimore, MD 21218 (USA)

[**] This project is supported by the DOE IPP program office. Supporting Information is available online from Wiley InterScience or from the author.

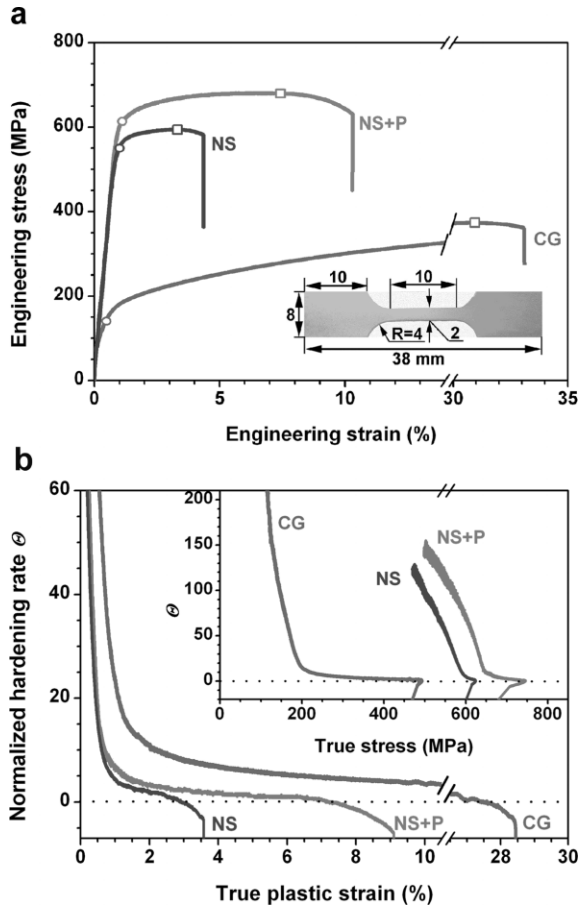

Figure 1. a) Tensile engineering stress–strain curves of the CG, NS, and NS+P samples. The open circles and squares mark the 0.2% yield strength and the uniform elongation, respectively. The inset shows dimension of the tensile sample with a thickness of 1 mm. *R* is the radius of the arc indicated by the arrow. b) Normalized work hardening rates, Θ, against the true strain. The inset shows curves of Θ against true stress.

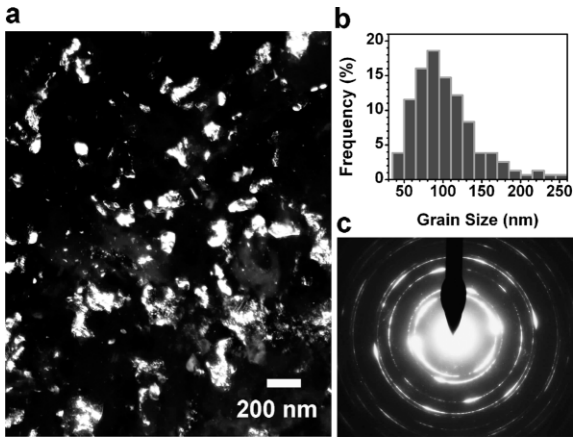

Figure 2. a) A dark-field TEM image, b) statistical grain size distribution, and c) a selected-area diffraction pattern from a 1 μm diameter area of an NS sample.

The mechanical behavior is controlled by microstructures. Figure 2a is a dark-field transmission electron microscopy (TEM) image of the NS sample, which shows irregularly shaped grains. Figure 2b shows the distribution of grain sizes measured from dark-field TEM images, with an average grain size of ca. 100 nm. Figure 2c is a selected-area diffraction pattern taken from a 1 μm diameter sample area. The clustered diffraction spots suggest that the grain boundaries are mostly low-angle type. The low-angle grain boundaries were caused by the relatively small plastic strain of cryorolling.

Aging the NS sample produced a high density of second-phase particles with an average interparticle distance of ca. 25 nm, but did not change the matrix grain size (Supporting Information, Fig. S1a–c). High-resolution TEM (HRTEM) and X-ray energy-dispersive spectrometry were used to identify the second-phase particles.[14–16] They were: coherent, spherical Guinier–Preston (G–P) zones with the same crystal structure as the matrix and a Zn/Mg atomic ratio of about 1:1; a semicoherent, plate-shaped, metastable hexagonal η′ phase with its habit plane {0002} parallel to matrix {111} and an atomic ratio of Zn/Mg = ~1.5:1; and a non-coherent, equiaxed, stable hexagonal η phase with an atomic ratio of Zn/Mg = 2:1. The average dimensions of these three types of precipitates were 4 nm, 4 nm × 10 nm (thickness × diameter), and 10 nm, respectively (Fig. 3a), and their densities were about 1×10^{15} m^{-2}, 4×10^{14} m^{-2}, and 1×10^{14} m^{-2}, respectively. The X-ray diffraction (XRD) pattern (Fig. 3b) reveals a small quantity of second-phase particles before aging (pattern CG), which redissolved into the matrix during the cryogenic rolling (pattern NS). Aging produced a large quantity of η′ and η particles (pattern NS+P).

The dislocation densities in the matrices of the CG, NS, and NS+P samples were estimated from XRD peak broadening (Fig. S2a and b)[17] as 1.0×10^{12} m^{-2}, 4.0×10^{14} m^{-2}, and 3.5×10^{14} m^{-2}, respectively. The lattice parameters of the matrices were 4.0599 Å (CG), 4.0599 Å (NS), and 4.0569 Å (NS+P). Thus, low-temperature aging only caused a slight recovery of the matrix.

The high dislocation density and fine grain size of the NS sample are primarily responsible for its improved strength over the CG sample, while the high density of second-phase particles in the NS+P sample is responsible for its improved strength over the NS sample. The strengthening by the second-phase particles would be higher than the measured ca. 12% increase in yield strength because the NS+P sample has lower solute over-saturation and dislocation density, both of which decrease the yield strength.

The enhanced uniform elongation in the NS+P sample is due to improvement in the work-hardening rate, Θ, through dislocation accumulation. Although high strain rate sensitivity can also enhance uniform elongation, our measurements did not show higher strain rate sensitivity in the NS+P sample. XRD analysis (Fig. S3a–c) reveals that after the tensile testing the dislocation density in the NS+P sample increased by 54% from 3.5×10^{14} m^{-2} to 5.4×10^{14} m^{-2}. In comparison, the dislocation density in the NS sample increased by only 8% from

ADVANCED MATERIALS

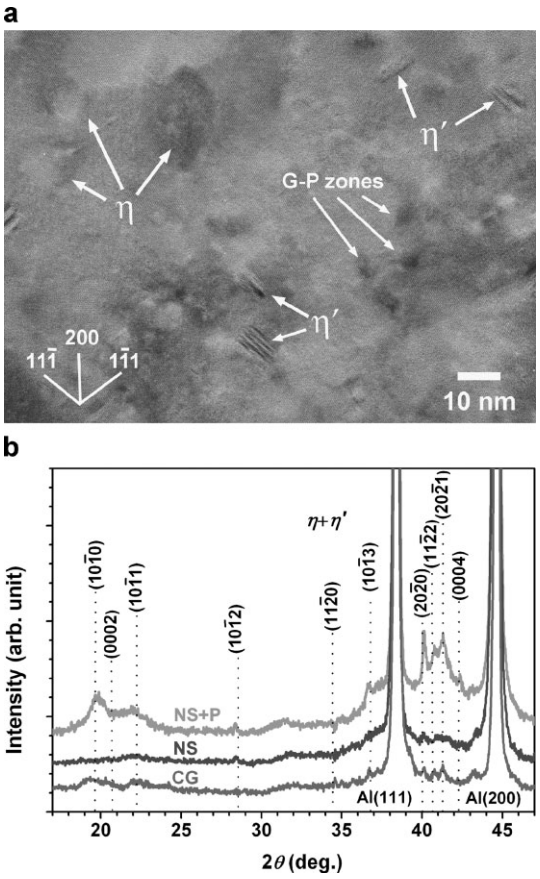

Figure 3. Precipitates in the CG, NS, and NS+P samples. a) HRTEM image along a <011> matrix zone axis of a NS+P sample showing spherical G–P zones, plate-shaped η′ phase, and equiaxed η phase. b) X-ray diffraction patterns showing the η′ and η phases in the CG, NS and NS+P samples.

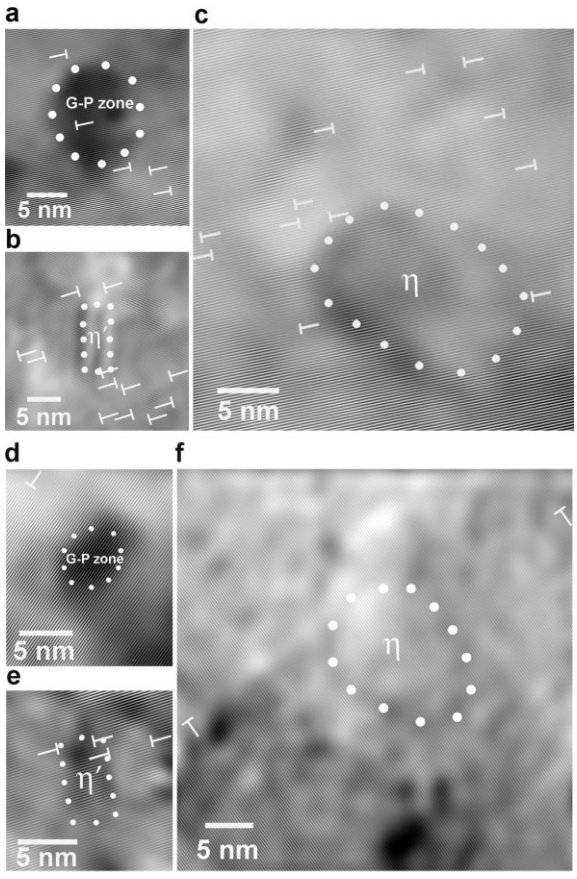

Figure 4. Typical {111} matrix planes obtained by inverse Fourier transformations of HRTEM images of an NS+P sample a–c) after and d–f) before tensile testing. a,d) The G-P zone and surrounding matrix. b,e) The meta-stable η′ particle and surrounding matrix. c,f) The stable η particle and surrounding matrix. The white dots mark the particle/matrix interfaces.

4.0×10^{14} m^{-2} to 4.3×10^{14} m^{-2}. The tensile test did not cause apparent changes in grain size. These data suggest that the improvement in Θ of the NS+P sample is primarily caused by the large amount of second-phase particles. However, the slight recovery of the matrix should also have some minor contribution to the high Θ.

To find out how the second-phase particles help with dislocation accumulation, we examined typical inverse Fourier transformations of HRTEM images of a NS+P sample. As shown in Figure 4a–c, after the tensile testing, a large number of dislocations exist around second-phase particles. Dislocations also exist inside the G–P zone. In contrast, before the testing very few dislocations exist around second-phase particles (Fig. 4d–f), and no dislocation is found inside them. The tensile testing did not affect the dislocation density at the edges of η′ and η particles, indicating that these dislocations were most likely generated by the lattice mismatch at the matrix/particle interfaces. These observations indicate that dislocations cut through the coherent G–P zones and accumulated around η′ and η particles. Therefore, the second-phase particles significantly hindered dynamic recovery and increased the dislocation storage capability, which increased the Θ. The second-phase particles also resisted dislocation slip, which increased the strength.

Other reported strategies for increasing the ductility of the nanostructured materials, such as bimodal grain sizes, sacrifice their strength or restrict their service conditions to low temperatures and high strain rates.[9,18–20] There have also been reports of nanostructured metals that have high strength and good ductility in the as-synthesized state.[21–25] However, these are only exceptions to the general observation that most nanostructured materials have very limited uniform ductility. Recent attempts to improve ductility of ultrafine-grained Al alloys via precipitation either decreased the yield strength or only increased the yield strength without improving ductility.[12,13,26]

In summary, we present a strategy to *simultaneously* increase the ductility and strength of bulk nanostructured materials. This strategy can be applied to many commercial alloy systems that use second-phase precipitation as a strengthening

mechanism (an example showing another case is presented in Fig. S4). It can also be used to design new alloys or nanocomposites by incorporating second-phase particles into the nanostructures. The cryogenic rolling employed in this study may be easily adapted to current industrial processes and hence has the potential for large-scale industrial applications of nanostructured materials. Finally, if the processing parameters are optimized, the ductility can be improved to rather high levels while simultaneously enhancing the strength (Fig. S4).

Experimental

A commercial 7075 Al alloy rod with a diameter of 15 mm was purchased in T6-treated state (i.e., aged at 120 °C for 48 h after solution treatment). It contained alloy elements of 5.60 wt % Zn, 2.50 wt % Mg, 1.60 wt % Cu, 0.50 wt % Fe, 0.40 wt % Si, 0.30 wt % Mn, 0.23 wt % Cr, and 0.20 wt % Ti. The alloy rod was machined into 6 mm × 10 mm × 10 mm bars and solution-treated at 500 °C for 5 h then quenched into liquid nitrogen (LN) to form a CG-solid solution sample. The CG sample was then immediately cryogenically rolled to form nanostructures with a grain size of ca. 100 nm. Before rolling, the rollers were partially immersed into LN and rotated for 10 min (Fig. S5), and the samples were pre-cooled in LN for 2 min. The total thickness reduction was 80 % after multiple rolling passes, with about 10 % thickness reduction per pass. After each rolling pass, the workpiece was dropped into LN automatically and kept for 2 min before the next rolling pass. To introduce second-phase particles, the cryogenically rolled NS sample was immediately aged, first at 50 °C for 5 h and then at 80 °C for 9 h in an argon atmosphere.

For tensile testing, all of the samples were cut and polished into dog-bone-shaped specimens with a gauge length of 10 mm and a cross section of 2 mm × 1 mm. Uniaxial tensile tests were performed at room temperature using a Shimazu Universal Tester at an initial quasi-static strain rate of 1.7×10^{-4} s^{-1}. Five specimens were used to obtain consistent stress–strain curves. The tensile tests on the CG and NS samples were finished within 1 h after quenching.

XRD measurements were carried out on a Scintag X-ray diffractometer operated at 1.8 kW and equipped with a Cu target. The XRD measurements (2θ from 15° to 50°) on the second-phase particles in the CG and NS samples were finished within 2 h after quenching. The gauge sections of tensile specimens were examined using XRD before and after tensile tests to study the change in dislocation density (see Fig. S6). The dislocation density was calculated from the grain size and microstrain obtained from XRD peak broadening [17, 27]. The error of the XRD-measured dislocation density value was less than 10 %. TEM and HREM were performed on a Phillips CM30 microscope operated at 300 kV and a JEOL 3000F microscope operated at 300 kV, respectively. The composition of the second-phase particles was determined by X-ray electron dispersive spectrometry under a Tecnai F30 scanning transmission electron microscope operated at 300 kV. The specimens for electron microscopy were prepared by mechanically grinding the samples to about 10 μm thickness. Further thinning to a thickness of electron transparency was carried out using a Gatan Dual Ion Milling System with an Ar^+ accelerating voltage of 4 kV and liquid nitrogen to cool the specimen.

Received: February 15, 2006
Final version: June 4, 2006

[1] R. Valiev, *Nature* **2002**, *419*, 887.
[2] C. C. Koch, *Scr. Mater.* **2003**, *49*, 657.
[3] J. R. Weertman, in *Nanostructured Materials: Processing, Properties and Applications* (Ed: C. C. Koch), William Andrews, Norwich, NY **2002**, p. 397.
[4] G. W. Nieman, J. R. Weertman, R. W. Siegel, *J. Mater. Res.* **1991**, *6*, 1012.
[5] H. Gleiter, *Prog. Mater. Sci.* **1989**, *33*, 223.
[6] R. Z. Valiev, Y. Estrin, Z. Horita, T. G. Langdon, M. J. Zehetbauer, Y. T. Zhu, *JOM* **2006**, *58 (April)*, 33.
[7] R. Valiev, *Nat. Mater.* **2004**, *3*, 511.
[8] G. E. Dieter, *Mechanical Metallurgy*, 3rd ed., McGraw-Hill, New York **1986**, p. 289.
[9] Y. Wang, M. Chen, F. Zhou, E. Ma, *Nature* **2002**, *419*, 912.
[10] Z. Budrovic, H. Van Swygenhoven, P. M. Derlet, S. V. Petegem, B. Schmitt, *Science* **2004**, *304*, 273.
[11] H. Van Swygenhoven, J. R. Weertman, *Scr. Mater.* **2003**, *49*, 625.
[12] Z. Horita, K. Ohashi, T. Fujita, K. Kaneko, T. G. Langdon, *Adv. Mater.* **2005**, *17*, 1599.
[13] Y. B. Lee, D. H. Shin, K. T. Park, W. J. Nam, *Scr. Mater.* **2004**, *51*, 355.
[14] G. Sha, A. Cerezo, *Acta Mater.* **2004**, *52*, 4503.
[15] R. Ferragut, A. Somoza, A. Tolley, *Acta Mater.* **1999**, *47*, 4355.
[16] M. Dumont, W. Lefebvre, B. Doisneau-Cottignies, A. Deschamps, *Acta Mater.* **2005**, *53*, 2881.
[17] Y. H. Zhao, X. Z. Liao, Z. Jin, R. Z. Valiev, Y. T. Zhu, *Acta Mater.* **2004**, *52*, 4589
[18] B. Q. Han, Z. Lee, D. Witkin, S. Nutt, E. J. Lavernia, *Metall. Mater. Trans. A* **2005**, *36*, 957.
[19] Y. Wang, E. Ma, R. Z. Valiev, Y. T. Zhu, *Adv. Mater.* **2004**, *16*, 328.
[20] Y. M. Wang, E. Ma, *Appl. Phys. Lett.* **2003**, *83*, 3165.
[21] L. Lu, Y. Shen, X. Chen, L. Qian, K. Lu, *Science* **2004**, *304*, 422.
[22] K. M. Youssef, R. O. Scattergood, K. L. Murty, J. A. Horton, C. C. Koch, *Appl. Phys. Lett.* **2005**, *87*, 091 904.
[23] R. Z. Valiev, I. V. Alexandrov, Y. T. Zhu, T. C. Lowe, *J. Mater. Res.* **2002**, *17*, 5.
[24] H. Li, F. Ebrahimi, *Appl. Phys. Lett.* **2004**, *84*, 4307.
[25] A. A. Karimpoor, U. Erb, K. T. Aust, G. Palumbo, *Scr. Mater.* **2003**, *49*, 651.
[26] J. K. Kim, H. K. Kim, J. W. Park, W. J. Kim, *Scr. Mater.* **2005**, *53*, 1207.
[27] Y. H. Zhao, K. Zhang, K. Lu, *Phys. Rev. B: Condens. Matter Mater. Phys.* **1997**, *56*, 14 322.